Geographia Technica, Vol. 21, Issue 1, 2026, pp 254 to 270

EXTRACTING THE SPACE-BORNE RADAR BACKSCATTERING RESPONSES OF DIFFERENT ROCK UNITS FOR GEOLOGICALLY MAPPING TAFILALET REGION IN MOROCCO

***Naoual El HAMMOUCH*[1,*], *Fatima El HAMMICHI*[1], *Hassan TABYAOUI*[1],**
***Ahmed GABER*[2], *Magaly KOCH*[3] & *Mohammed MOURJANE*[1]**

DOI: 10.21163/GT_2026.211.17

ABSTRACT

Rock surfaces affected by weathering usually exhibit distinctive spectral characteristics compared to their unaffected counterparts. Furthermore, certain rock units, particularly those with white color, such as carbonate rocks, evaporites, and white sandstone, have very similar spectral responses. This makes it extremely difficult to classify data using only optical remote sensing. On the other hand, by capturing these rock units' radar backscattering responses, completely polarimetric Synthetic Aperture Radar (PolSAR) data offer important insights about their external geometry and surface roughness. Their external geometries differ according to the different lithologies and geological formations since every rock unit has specific physical and chemical weathering characteristics. Consequently, such information facilitates improved classification and mapping. To achieve more accurate classification and geological mapping, this research uses fully polarimetric ALOS/PALSAR-2 data to extract the unique radar scattering responses of rock units along the Tafilalet region. The utilized imagery is decomposed into entropy, alpha, and anisotropy (H-α-A) distribution, Pauli decomposition, Wishart supervised classification with eight classes, and their polarization signatures (PS). Additionally, field validation is conducted to verify the classification outcomes. The Wishart supervised classification based on Synthetic Aperture Radar (SAR data), exhibits alignment with the geological map, surpassing the accuracy achieved using ASTER optical data. These findings indicate that the rocks within the Tafilalet study area have undergone varying degrees of weathering, resulting in distinct the surface roughness and corresponding scattering mechanisms of Synthetic Aperture Radar (SAR) data, which facilitate improved classification and mapping efforts.

Keywords: *Radar images, Space-based; Supervised classification; Geologic mapping; Morocco.*

1. INTRODUCTION

Synthetic Aperture Radar (SAR) is essentially a useful imaging radar method for achieving high spatial resolution from space-based platforms. Imaging radar has developed as a useful and indispensable earth remote sensing technique since the successful 1978 launch of the SEASAT satellite, which was equipped with a Synthetic Aperture Radar (SAR). Several space-borne polarimetric SAR (PolSAR) systems, notably the Advanced Land Observing Satellite (ALOS), TerraSAR-X, and RADARSAT-2, have since been launched with success. These three satellites, each equipped with Polarimetric SAR (PolSAR) systems operating at a different frequency, provide a

---

[1] *Geo-Resources and Environment Laboratory, Sidi Mohammed Ben Abdellah University, Fez, Morocco;*
[*] *Corresponding author naoual.elhammouch@usmba.ac.ma (N.H), fatima.elhammichi@usmba.ac.ma (F.E.H), has-san.tabyaoui@usmba.ac.ma (H.T), mourjanemohammed@gmail.com (M.M)*
[2] *Faculty of Science, Port Said University, Egypt; ahmedgaber_881@hotmail.com (A.G)*
[3] *Dept. Earth & Environment, Boston University, USA; mkoch@bu.edu (M.K).*

comprehensive data source for Earth environmental monitoring, including applications such as hazard monitoring, soil moisture estimation, snow cover and snow content assessment, water and forest detection, urban planning, ocean current and wave dynamics detection, and evaluation of geophysical constraints and changes.

Radar polarimetry, derived from polarimetry and remote sensing principles, analyzes the vector character of electromagnetic waves (Deschamps, 1951; Boerner et al., 1985; Boerner, 2004). The goal is to characterize targets based on their responses to different transmission and reception polarizations. The following references provide a detailed history of radar polarimetry, Cloude and Pottier (1996), Boerner and Cloude (2002), Oliver and Quegan (2004), Lee and Pottier (2009), López-Martínez and Pottier (2021).

In land cover classification, selecting an effective classification algorithm is an essential area for research (Lu and Weng, 2007). The Wishart classification system is the most frequently employed polarimetric synthetic aperture radar (SAR) classification technique (Lee et al., 1994). Furthermore, the polarization signature, which is provided as a 3D graphic, is extremely useful for classification. This visualization technique thoroughly elucidates the polarization powers of an object by displaying variations in the orientation and ellipticity angles of the polarization ellipse (Vanzyl et al., 1987).

In the context of geological mapping, optical satellite sensors have some limitations. Optical sensors usually provide surface-level data on geological formations and structures, making them inefficient for detailed geological mapping in vegetated areas. However, radar sensors provide considerable advances in geological mapping. Polarimetric data make it possible to characterize the physical properties of geological materials in detail, including internal structure, composition, and roughness. Polarimetric data can be combined with additional geological information to overcome the limitations of optical data, resulting in a more exact and comprehensive classification of geological formations.

The external geometry of different rock units reveals information about their spatial distribution, structural properties, and morphological features. Researchers use remote sensing techniques, such as satellite imagery and aerial photography, to delineate boundaries between disparate rock units, identify structural features, folds and faults, characterize landforms influenced by the underlying geology, and quantify morphological parameters that indicate distinct rock types. Integrating information from exterior geometry with complementing geology data sets enables radar remote sensing to permit more precise and complete classifications, improving our understanding of the earth's dynamic geologic processes and spatial diversity across varied terrains.

In this study, polarimetric information from various surface features and rock units was extracted and correlated with geological classifications. Subsequently, supervised classification was performed using the statistical properties of polarimetric SAR. Notably, the polarization signatures of these distinct geological units were first defined within the study area, facilitating enhanced discrimination.

2. STUDY AREA

The study area is situated in southeastern Morocco, limited by the coordinates 4° 30' W & 31° 15' N and 3° 45' W & 30° 45' N (**Fig. 1**). It located in the southern Tafilalet valley, surrounded by the Kem Kem plateau to the south and the Hamada du Guir to the east. The valley is underlain by a Paleozoic basement and covered by Cretaceous and Tertiary sedimentary rocks from the Kem Kem plateau. A continental Miocene complex capped by a Pliocene limestone cover characterizes the Hamada du Guir. The drainage system is influenced by the Oued Ziz corridor and its tributaries, which are affected by winds transporting Saharan sand and dust towards the northeast, contributing to the Erg Chebbi dune system. Altitudes range from around 730 m a.s.l. on the plain to more than 880 m of the dune crests and 950 m in the Paleozoic reliefs west of Oued Ziz. The Kem Kem plateaus and Hamada du Guir feature sub-tabular topography with a moderate northward slope. Altitudes reach about 1000 m in the Hamada de Guir and 860 m in the Kem Kem, with a semi-desert environment and a large river network (Joly, 1962). The study area comprises an arid climate with infrequent precipitation. Vegetation is sparse, except for the Marzouga palm grove.

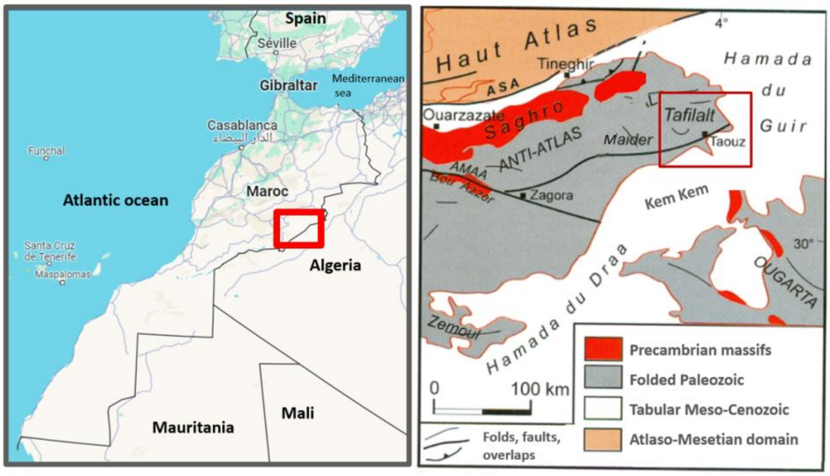

Fig. 1. Location of the study area on the structural map of Morocco at scale 1:2,000,000 [20]. Geological map of SE Morocco at scale 1:1,000,000.

3. DATA AND METHODS

To facilitate the comparison of spectral responses between radar polarimetry data and optical sensors, a preliminary analysis was conducted using the Advanced Spaceborne Thermal Emission and Reflection Radiometer (ASTER) sensor to identify distinct unit classes within the study area. Five ASTER Level 1B "radiance-at-sensor" data sets covering the region of interest were acquired from the Earth Resources Observation and Science (EROS) Center of the National Aeronautics and Space Administration (NASA) (https://LPDAAC.usgs.gov). These data sets underwent preprocessing steps that included resampling, stacking, mosaicking, clipping, radiometric calibration, and atmospheric correction. Subsequently, radiometric calibration was performed to convert the digital numbers (DNs) in the original image pixels (16-bit integers) into physical radiance values. Atmospheric correction was applied to the VNIR and SWIR bands using the Fast Line-of-sight Atmospheric Analysis of Spectral Hypercubes (FLAASH) algorithm (Cooley et al., 2002). An unsupervised classification was carried out using the K-means clustering algorithm with an initial 12 classes and 7 iterations. Field investigations in conjunction with a supervised classification using the maximum likelihood classifier (MLC) for parametric input data revealed that the initial 12 unsupervised classes could be refined into only 8 supervised classes (**Fig. 2**). Due to the limited availability of ground reference samples in several inaccessible areas of the Tafilalet region, a comprehensive quantitative accuracy assessment could not be performed. The reliability of the eight supervised classes was therefore confirmed by field observations, lithological consistency, and analysis of polarimetric scatter mechanisms.

The Radar data used in this study were collected via the phased array L-band Synthetic Aperture Radar (PALSAR-2) onboard the Advanced Earth Observation Satellite (ALOS) in ascending orbit mode with full polarization (HH, HV, VV, VH). Acquired on November 29, 2009, the data exhibited a 2.79 m azimuthal resolution and a 4.81 m look direction resolution. JAXA, Japan supplied the data in L-band, product level 1.1, Single Look Complex (SLC) format, which were accessible through the ALOS-2 6th RA PI-3131 agreement. Preprocessing of SAR data entailed geocoding, speckle filtering using the adaptive Lee filter with a 7 × 7 window size (Lee et al., 2008), and conversion to a coherency matrix (T matrix).

Furthermore, to aid in the comprehension of terrain feature scattering behavior, the fully polarized data acquired from ALOS PALSAR-2 was decomposed into entropy (H), alpha (α), and anisotropy (A) values. Depolarizing elements are demarcated using entropy, whereas alpha angle differentiates surface elements with volume diffusion from those with single or double-bounce diffusion. Entropy and alpha values can be used to characterize weathering zones based on physical surface attributes. Anisotropy, a quantity that complements entropy, becomes relevant when entropy is considerably elevated (Woodhouse, 2006).

Furthermore, the Pauli decomposition, widely used and based on the coherence matrix. Each parameter has a distinct physical meaning. In specifically, the diagonal elements |HH + VV|, |HH-VV|, and |HV| harbor the most valuable polarimetric data. The Pauli RGB composite image, constructed from the intensities |HH - VV| (red), |HV + VH| (green), and |HH + VV| (blue), provides visual discernment of the three primary diffusion mechanisms in the region under investigation (Qi et al., 2012).

Consequently, the Wishart supervised classification was performed using the training domains specified in the consistency matrix, as explained by (Varghese and Joshi, 2014). Furthermore, the polarization signature (PS) was extracted to identify between the different land cover classes, providing a three-dimensional visual depiction of each target's backscatter properties. While polarimetric signatures have been reported in other arid regions of North Africa (e.g., Saharan and Atlas studies), this study is the first to systematically define them in the Tafilalet region, demonstrating the added value of full-polarimetric SAR for lithological mapping in structurally complex areas.

Field validation was conducted to verify the classification results, which involved collecting rock samples from several locations within the study area. Field validation consisted of qualitative observations carried out at accessible places, supported by the official 1:100,000 geological map and high-resolution Google Earth images. Although no GPS devices were utilized, the geolocation accuracy supplied by Google Earth (usually a few meters) was adequate to verify lithological limits and support the interpretation of polarimetric diffusion behavior.

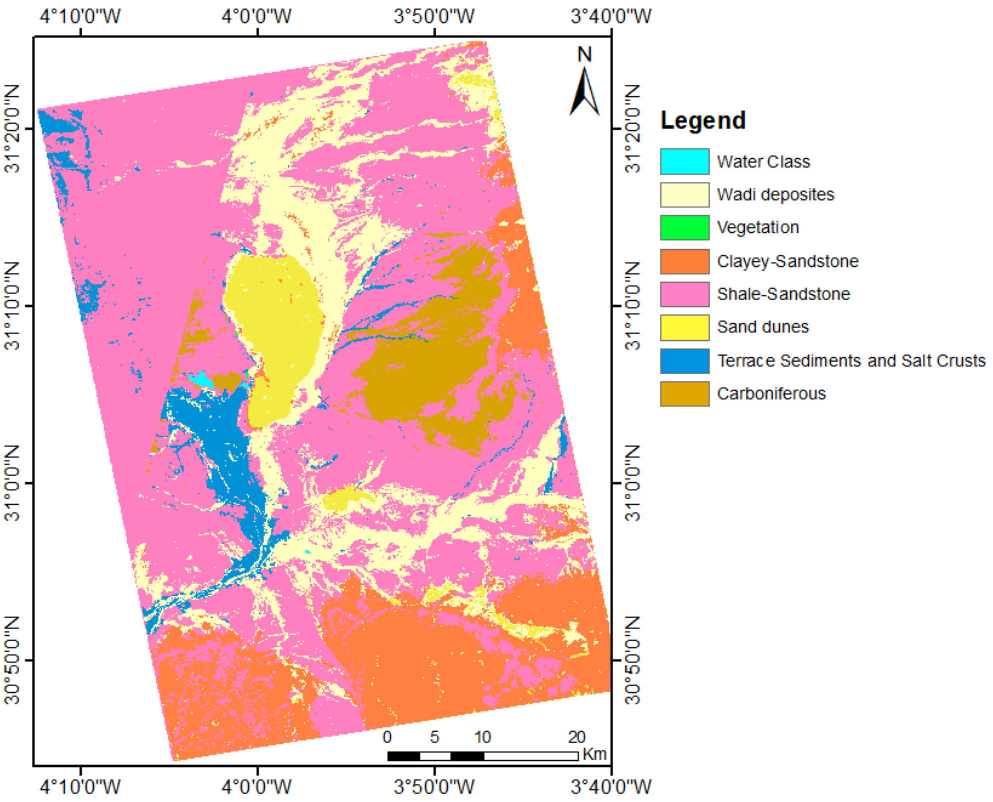

Fig. 2. Supervised classification map obtained from the ASTER optical data.

4. RESULTS

4.1. Entropie (H)

Entropy values range from 0 to 1 (Cloude and Pottier, 1997). **Fig. 3** shows the entropy (H) image, dividing the study area into three main regions: light blue representing low entropy, yellow representing medium entropy, and red representing high entropy. Regions with H = 0 (dark blue) correspond to flat, bare soils with low surface roughness, mainly found in the Oued Ziz valley. Areas with medium entropy (yellow) exhibit rougher surfaces with weathered rocks that enhance depolarized wave scattering. High entropy zones (red) coincide with argillic alteration areas containing clay minerals, particularly on the crests of the Erg Chebi sand dunes. The constant wind in the study area produces slightly rough water surfaces, resulting in a single-bounce scattering mechanism and low entropy values.

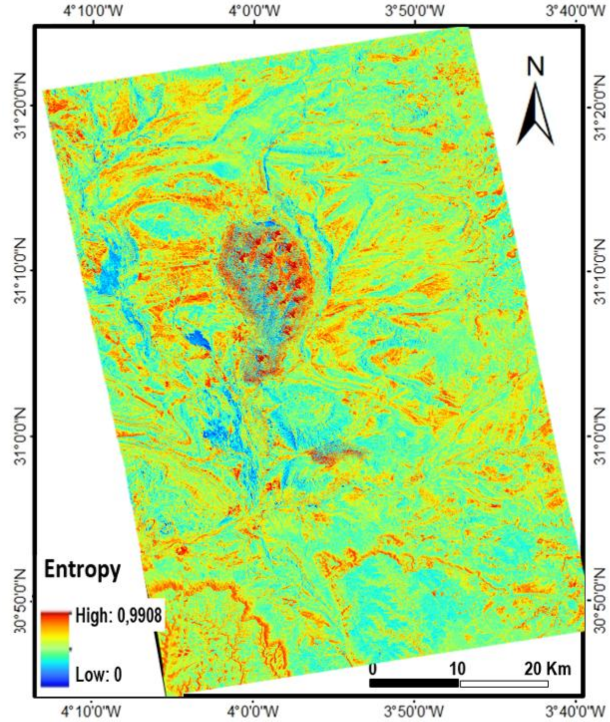

Fig. 3. Spatial variation of Entropy decomposition (H) along the study area.

4.2. Angle alpha (α)

The alpha angle (α) ranges from 0° to 90°, reflecting the nature of the scattering mechanism. **Fig. 4** distinguishes three main classes. Regions shown in dark blue have a very low alpha angle, below 10°, corresponding to surfaces with negligible specular backscatter. These surfaces, mainly weathering deposits, are located in the Oued Ziz valley and its tributaries. Surfaces with moderate backscatter appear light blue and correspond to alteration zones of the Kem Kem plateau's tabular reliefs, where ground observations indicate dominant advanced argillaceous weathering. Yellowish areas exhibit alpha angles between 30° and 50°, reflecting high soil and surface exposure and associated with volume scattering. The highest alpha angle class, exceeding 60°, represents dominant dihedral scattering and is observed as yellowish points on clay-based sand dune ridges. L-band Polarimetric SAR (PolSAR) data, oriented along the radar line of sight, allow accurate characterization of terrain features using the alpha angle.

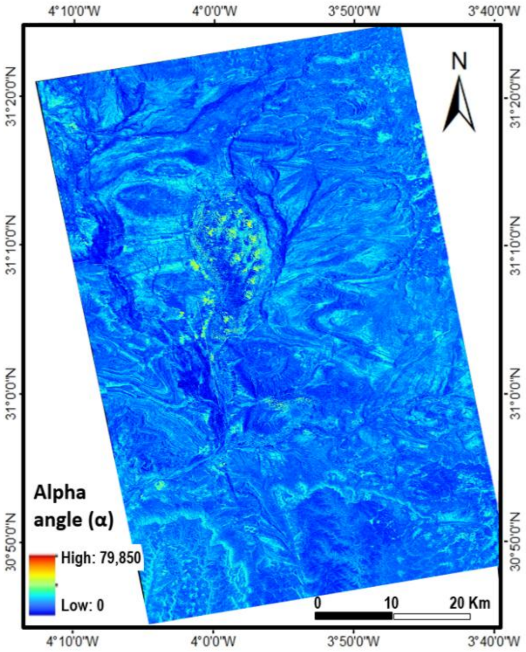

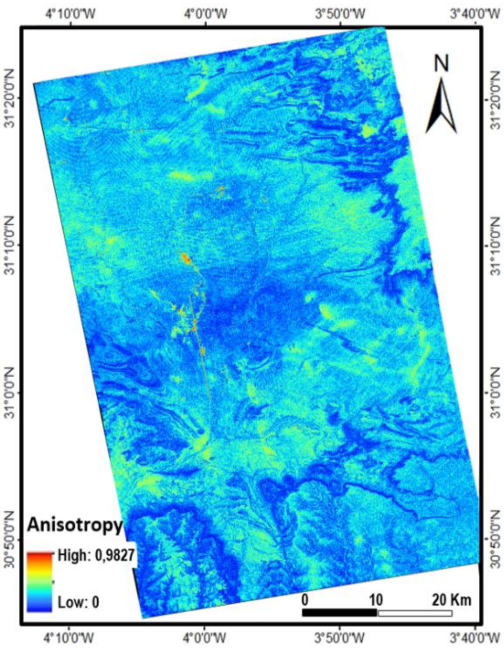

Fig. 4. Spatial variation of Alpha angle

Fig. 5. Spatial variation of anisotropy (A).

4.3. Anisotropie (A)

Anisotropy (A) varies across the study area, reflecting the relative contribution of different scattering mechanisms. Areas of low anisotropy (dark blue) correspond to surfaces where two scattering mechanisms contribute equally. Medium anisotropy (light blue to yellowish) indicates surfaces where dominant scattering mechanisms occur with roughly equal probability, independent of entropy values, surface dielectric properties, or incidence angle variations (Cloude, 1999; Mattia and Le Toan, 1999). This shows that anisotropy is a useful indicator of surface roughness variations. High anisotropy values ($A \approx 0.6$), typically shown in orange to red, represent surfaces dominated by a single scattering mechanism, such as water surfaces with significant Bragg scattering. Wet surfaces with near-unity anisotropy were not observed in the study area (**Fig. 5**).

4.4. Alpha-Entropy decomposition

The Alpha-Entropy (H–α) decomposition, derived from an eigenvalue-based target decomposition, reveals overlapping classes that predominantly exhibit surface scattering with intermediate alpha values and comparatively high entropy values under full-polarization mode (**Fig. 6a**). Minimal alpha values correspond to surface scattering typical of flat surfaces, while volume scattering indicates surfaces composed of anisotropic particles.

In the study area, Zones 9 and 6 display surface diffusion processes at low and moderate entropy (H), respectively, within a spatial range of alpha angle values below 42.5°. Zone 9 delineates the drainage system of the Ziz plain, including temporary lakes (Dayat Tamazguidat) and saline crusts of the sebkhas, which occur west of the Erg Chebi in depressions filled with fine, highly saline sediments, reflecting low precipitation and high evaporation. Zone 6 exhibits increased entropy due to variations in surface roughness and reduced alpha angles. This zone comprises diverse continental land surfaces from the Quaternary, flat limestone-to-flint surfaces of the Kem Kem plateau from the Upper Cretaceous, and Pliocene calcareous-sandstone slabs covering the Hamada de Guir.

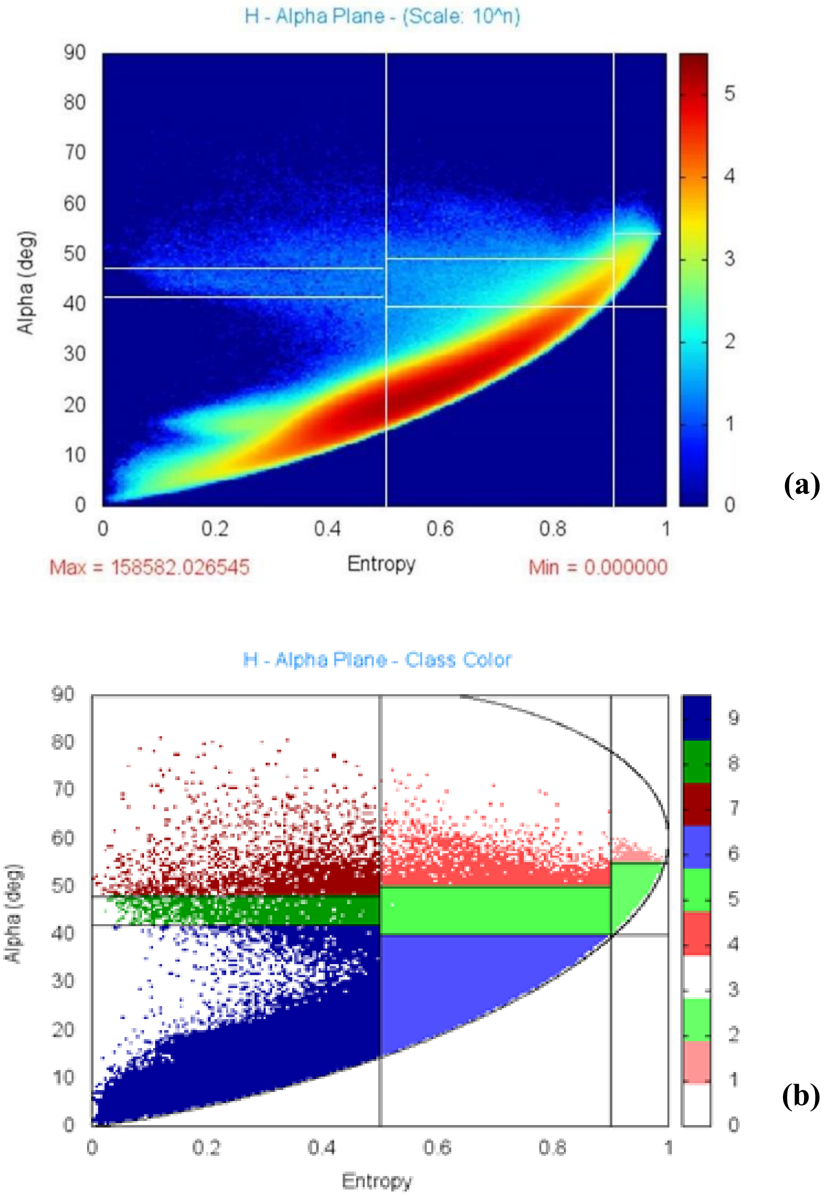

Fig. 6. (a) α-H distribution for scattering mechanism. (b) α-H scattering mechanism identification plane of the study area.

Zones 8 and 5 show predominantly dipolar scattering patterns corresponding to low and moderate entropy values, originating from anisotropic scatterers within the Paleozoic basement clay-sandstone interfaces, exhibiting moderate correlation in their orientations. Zones 7 and 4 correspond to multiple scattering events at low and moderate entropy, respectively, with PolSAR pixels ranging from 47.5° to less than 62°. Zone 7 includes Cretaceous gypsum marls forming cliffs at the Kem Kem plateau edges and Paleozoic relief crests, while sand dunes on Erg Chebi show multiple scattering under low entropy conditions. Zone 4 represents the escarpments of the Hamada de Guir, including Mio-Pliocene conglomerates and sandstones. As entropy increases from 0.6 to 0.9 in this area, alpha values decrease correspondingly to around 55°.

High entropy diffusion processes dominate Zones 2 and 1, resulting from single scattering events by anisotropic particle clouds. Scant vegetation and specific geological formations, particularly clay alteration zones and sand dune crests, further influence these scattering patterns.

The strength of this approach lies in estimating the observed environment type based on a physical interpretation of canonical scattering mechanisms. This is evident in **Fig 6b**, where variations in polarimetric characteristics enable meaningful classification of natural environments. Additionally, the H–α color composite provides detailed information on the polarimetric properties of the scene (**Fig. 7**), with the false-color image highlighting additional rock units and lineaments not visible on the geological map.

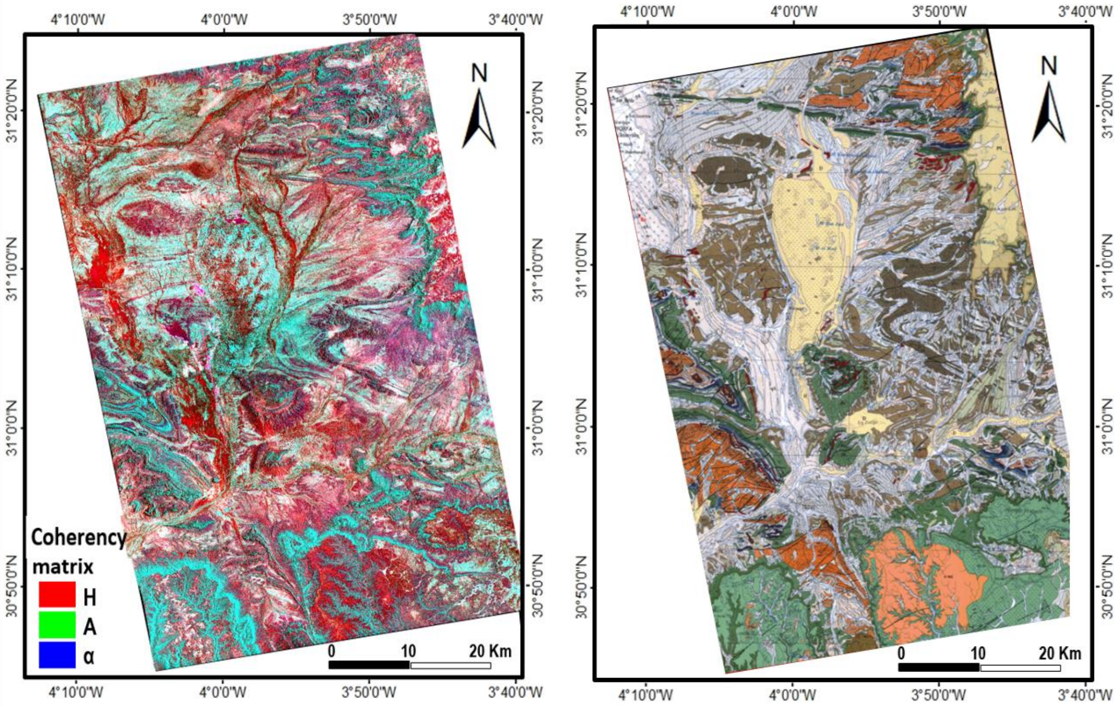

Fig. 7. The Cloude–Pottier decomposition (Red is entropy (H), green is anisotropy (A), blue is alpha angle (α)) and corresponding detailed geological map of Tafilalet-Taouz at 1/200000 (Destombes and Hollard, 1975).

4.5. Pauli RGB

The Pauli RGB image of the study area is presented as a class map, revealing several distinct main units (**Fig. 8**). The central part of the image, corresponding to the Tafilalet plain intersected by the Oued Ziz, displays these units. Blue areas indicate surface scattering, exemplified by the dry valley of Oued Ziz. In this region, the polarimetric channel |HH+VV| shows a high amplitude relative to others, reflecting a weak |HV| amplitude and a phase difference between |HH| and |VV| close to zero. Olive-green dots with elevated green and red components correspond to high |HV| values, indicating volume scattering associated with the crests of sand dunes in Erg Chebi.

In the southern and eastern regions, including the Kem Kem plateau and the Hamada of Guir, the Pauli decomposition shows pronounced multiple scattering, indicative of highly rugged surfaces. Areas appearing black in the Pauli RGB image represent Bragg scattering, where radar signals undergo complete dispersal or attenuation

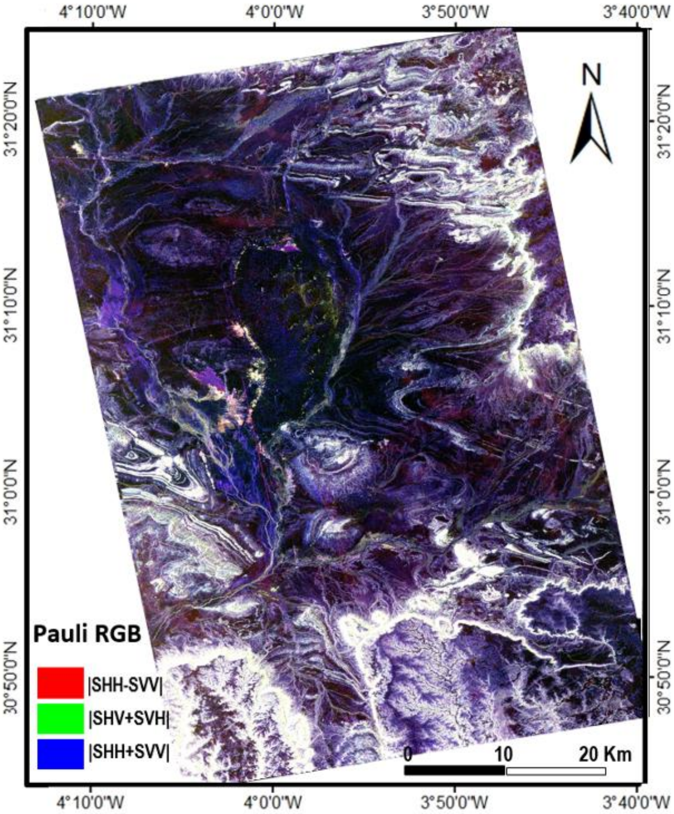

Fig. 8. Pauli-decomposition of the study area.

4.6. The supervised classification of Wishart

The Supervised Wishart Classification identifies eight distinct classes across the study area (**Fig. 9**). This algorithm was applied within each scattering category, producing classes that group pixels exhibiting the same diffusion mechanism (Lee et al., 1999; Lee et al., 2004). The resulting classification effectively distinguishes surface types and scattering behaviors, providing a detailed characterization of the geological and geomorphological units in the Tafilalet plain and surrounding regions.

4.7. Polarization Signatures

The co-polarization and cross-polarized signatures derived from ALOS/PALSAR-2 of distinct geological units within the Tafilalet plain, which include dune-associated coarse sands, clayey sandstone, sandstone and conglomerates, shale-sandstone, exposed limestone surfaces, fine-grained erosion sediments (aeolian sands), terrace sediments and salt crusts, water bodies, and vegetation (**Fig. 10**).

Sand dunes. The pedestal height range of this class extends from a maximum of -26.54 dB to a minimum of -31.21 dB for the co-polarized channel and from a maximum of -27.88 dB to a minimum of -35.68 dB for the cross-polarized channel. The mean values of its alpha (a°), entropy (H), and anisotropy (A) are 26.302, 0.623, and 0.368, respectively, with standard deviations of 6.286, 0.110, and 0.114 (**Table 1**). Its polarization response exhibits angles near ($\psi = 0°$), indicating a dominance of vertically aligned scatterers. The maximum response is higher at HH than at VV, with the maximum of this signature shifted from the horizontal to the vertical position. The ellipticity angle is 0°, denoting linear polarization.

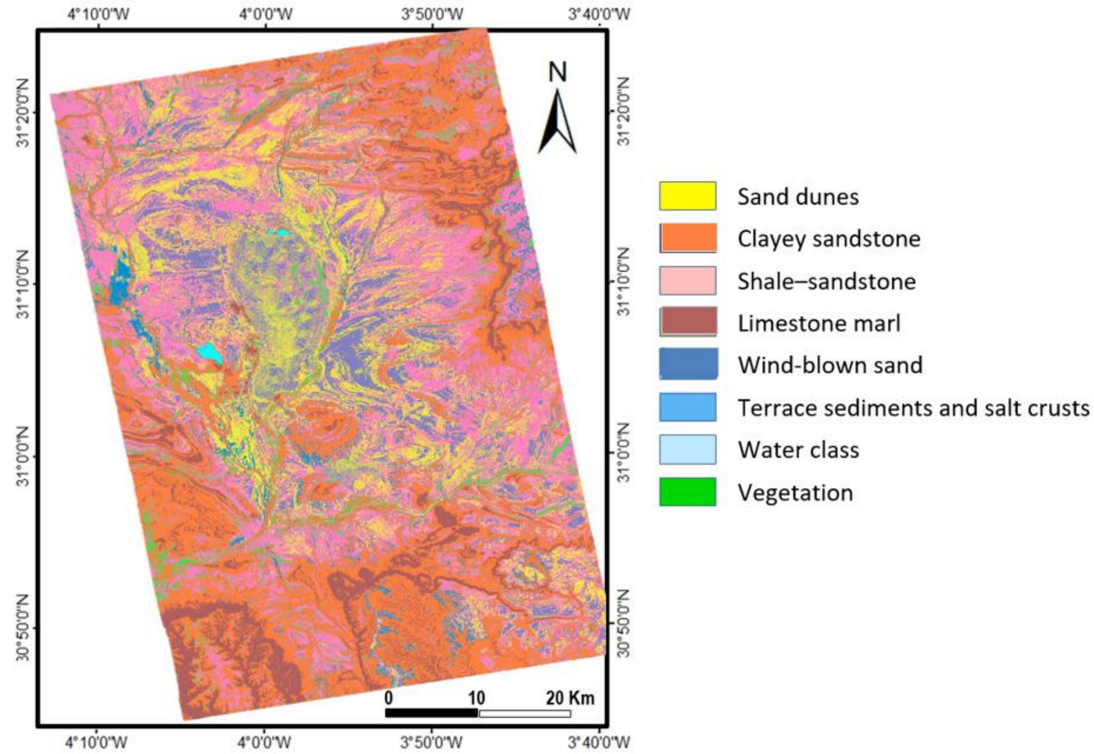

Fig. 9. The supervised Wishart classification of the study area.

Clayey sandstone. The pedestal height of this class exhibits a maximum of -6.68 dB and a minimum of -37.11 dB for the co-polarized channel and a maximum of -6.77 dB and a minimum of -42.59 dB for the cross-polarized channel, values which closely approach the noise floor system of the PALSAR sensor. The mean values of its alpha (a°), entropy (H), and anisotropy (A) are 21.482, 0.511, and 0.325, respectively, with standard deviations of 6.212, 0.123, and 0.120 (**Table 1**). The polarization response reveals angles near ($\psi = 90^o$), signifying a preponderance of vertically oriented scatterers, and exhibits a maximum response higher at VV than at HH, with the maximum of this signature shifted from the vertical to the horizontal position. The ellipticity angle of 0° indicates linear polarization.

Shale–sandstone. The pedestal height of this category exhibits a maximum of -17.30 dB and a minimum of -25.32 dB for the co-polarized channel and a maximum of -18.54 dB and a minimum of -30.33 dB for the cross-polarized channel. Analysis of the polarization response reveals that angles approximating ($\psi = 0^o$) denote a preponderance of scatterers oriented vertically. Furthermore, the maximum response is greater for HH than for VV, exhibiting a shift from the horizontal to the vertical position for the maximum of this signature. The ellipticity angle of 0° indicates linear polarization.

Limestone marl. The baseline height for this class exhibits a maximum value of -5.26 dB and a minimum value of -21.66 dB for the co-polarized channel, while the cross-polarized channel presents a maximum value of -7.06 dB and a minimum value of -29.52 dB. The mean values of its alpha (a°), entropy (H), and anisotropy (A) are 23.177, 0.559, and 0.278, respectively, with corresponding standard deviations of 6.726, 0.127, and 0.120 (as detailed in **Table 1**). The polarization response reveals that angles approaching ($\psi = 90°$) signify a preponderance of vertically oriented scatterers. The maximum response is more pronounced at VV than at HH, exhibiting a shift from vertical to horizontal alignment. The ellipticity angle of 0° indicates linear polarization characteristics.

Wind-blown sand. The pedestal height for this class exhibits a maximum value of -21.61 dB and a minimum value of -30.07 dB for the co-polarized channel. The cross-polarized channel exhibits a maximum value of -23.12 dB and a minimum value of -33.83 dB. Statistical analysis reveals mean values of 18.343, 0.473, and 0.342 for alpha (a°), entropy (H), and anisotropy (A), respectively. Standard deviations for these parameters are 3.563, 0.075, and 0.106, respectively (**Table 1**). The polarization response indicates a predominance of vertically oriented scatterers (ψ = 0º), with a maximum response observed at HH polarization. This maximum response is shifted towards the vertical position compared to VV polarization. The ellipticity angle of 0° implies linear polarization.

Terrace sediments and salt crusts. The pedestal height for this class spans from a maximum of -21.19 dB to a minimum of -43.33 dB for the co-polarized channel, while ranging from -14.28 dB to -32.34 dB for the cross-polarized channel. The polarization response indicates that angles approaching 90 degrees, signifying a preponderance of vertically oriented scatterers, yield the highest maximum response for the VV polarization relative to the HH polarization. Notably, the maximum of this signature exhibits a shift from the vertical to the horizontal plane for the HH polarization.

Water class. The pedestal height of this class exhibits a maximum of -11.76 dB and a minimum of -27.34 dB for the co-polarized channel, while the cross-polarized channel exhibits a maximum of -14.28 dB and a minimum of -32.34 dB. The mean values of its alpha (α°), entropy (H), and anisotropy (A) are 16.6, 0.296, and 0.350, respectively, with standard deviations of 2.772, 0.089, and 0.114 (**Table 1**). The polarization response indicates a predominance of vertically oriented scatterers, with a stronger response at VV than at HH. This suggests a deviation of the maximum response from the vertical to the horizontal position. The ellipticity angle is 0°, indicating linear polarization, which is consistent with the conventional Bragg scattering mechanism for water.

Vegetation. The pedestal height for this class exhibits a maximum of -16.63 dB and a minimum of -25.89 dB for the co-polarized channel, and a maximum of -17.91 dB and a minimum of -30.06 dB for the cross-polarized channel. The mean values of its alpha (a°), entropy (H), and anisotropy (A) are determined as 18.343, 0.603, and 0.363, respectively, with corresponding standard deviations of 6.944, 0.118, and 0.117 (refer to **Table 1** for detailed values).

Table 1.

The SAR scattering responses of all classes covering the study area.

Classes	**Area Km^2**	**SAR Scattering Mechanism**					
		Alpha(a)		**Entropy (H)**		**Anisotropy (A)**	
		Mean	**STD**	**Mean**	**STD**	**Mean**	**STD**
Sand Dunes	609,1	36,302	6,286	0,623	0,110	0,368	0,114
Clayey sandstone	506,2	21,482	6,212	0,511	0,118	0,325	0,120
Shale–sandstone	811,3	19,738	4,022	0,474	0,080	0,367	0,112
Limestone marl	359,9	23,177	6,726	0,559	0,127	0,278	0,119
Wind-blown Sand	203,4	18,343	3,563	0,473	0,075	0,342	0,106
Terrace sediments and salt crusts	119,4	12,203	3,350	0,332	0,078	0,353	0,111
Water	7,3	16,623	2,772	0,296	0,0819	0,350	0,114
Vegetation	144,7	25,269	6,944	0,603	0,123	0,363	0,117

***Note**: Values are expressed in decibels (dB). STD = standard deviation.*

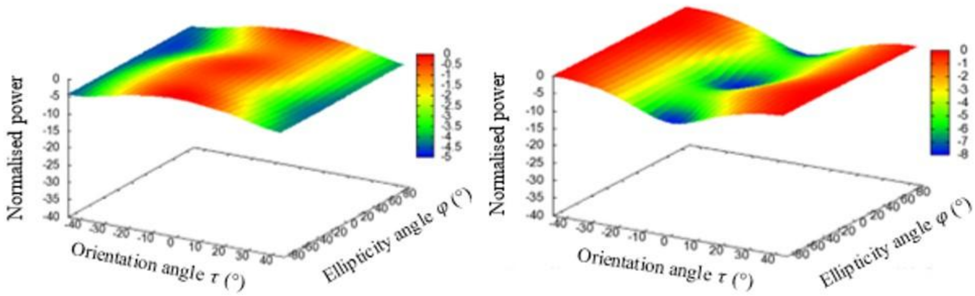

(a) *Sand Dunes* **(b)**

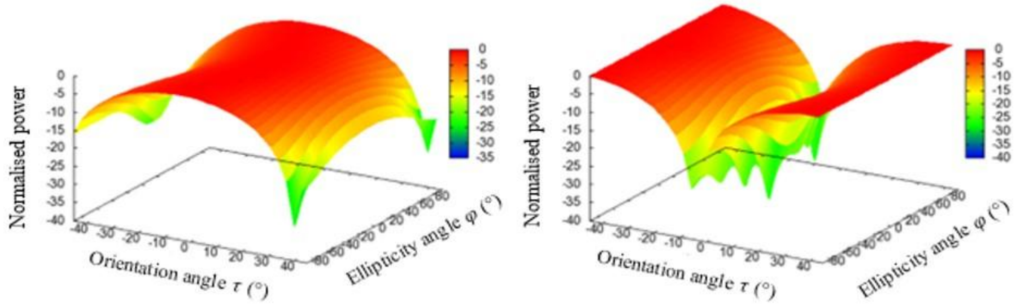

Clayey sandstone

(c) **(d)**

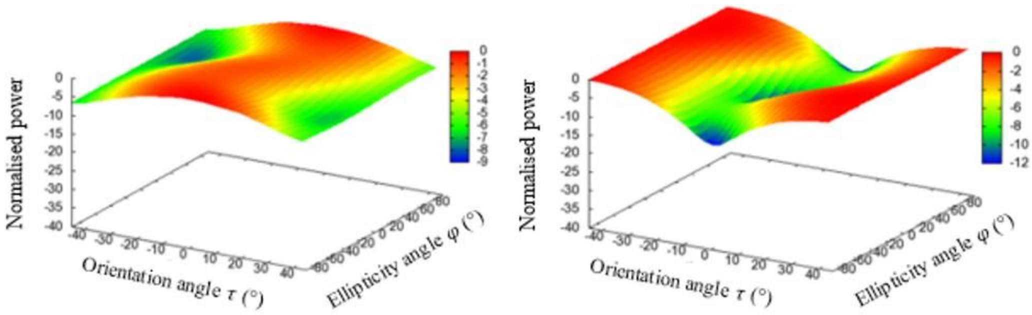

(e) **(f)**

Shale–sandstone

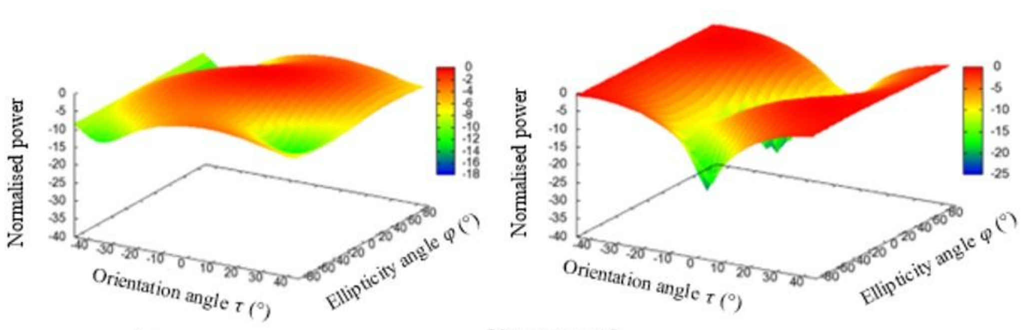

(g) *Limestone marl* **(h)**

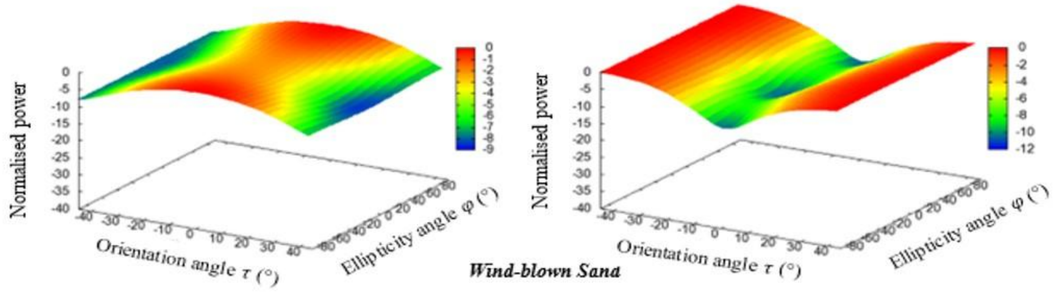

Wind-blown Sand

(i) **(j)**

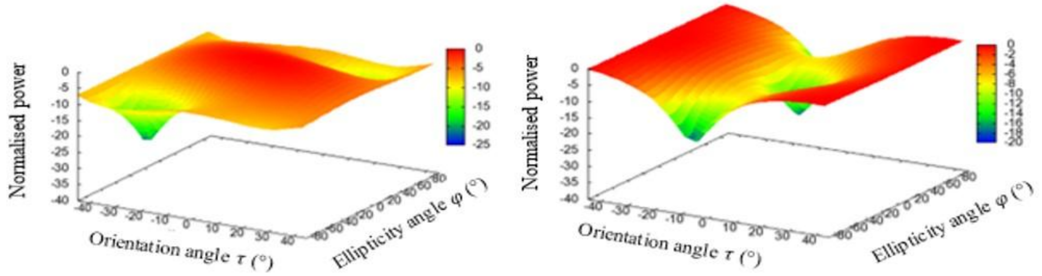

Terrace sediments and salt crusts

(k) **(l)**

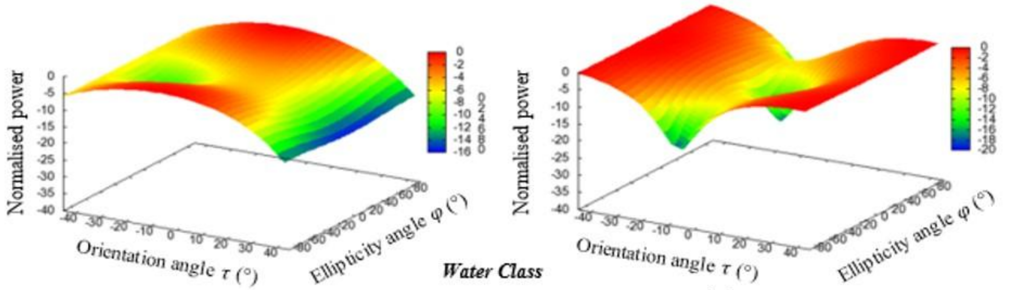

Water Class

(m) **(n)**

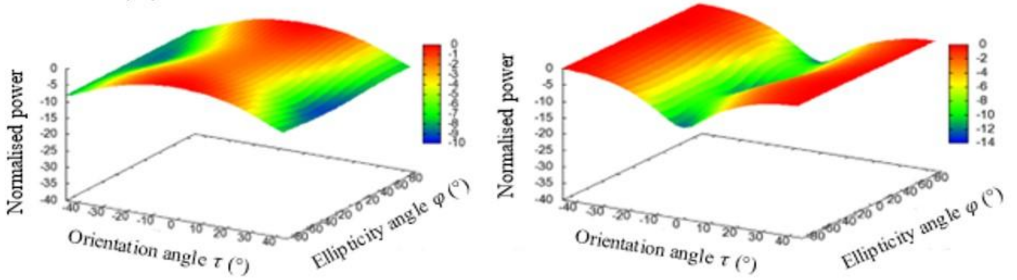

Vegetation Class

(o) **(p)**

Fig. 10. Polarization signatures of different geological units of the Tafilalet : (a,c,e,g,i,k,m,p) Co-polarization signature and (b,d,f,h,j,l,n,o) Cross-polarization signature.

5. DISCUSSION

The investigated region, a desert characterized by prominent outcrops devoid of vegetation cover, exhibits four contrasting geomorphic domains. To the west and north, regions with substantial relief, akin to the Appalachian Mountains, correspond to the Paleozoic sequence dating from the Ordovician to Devonian periods. The central area encompasses the alluvial plain of Oued Ziz, overlying bedrock belonging to the later Paleozoic folded series of Lower Carboniferous to Visean age, which is further concealed by a notable dune system, namely the Erg Chebbi and Erg Znaigui. Extending southward and eastward are the Kem Kem Plateau and the Hamada de Guir. The exposed terrains comprise Ordovician sandstones (First Bani, Ktaoua Formation, and Second Bani), Silurian clay-limestone sequences, limestones and marly limestones (Erfoud Group, Tafilalet Group), and Devonian sandstones (Taouz Group), along with detrital deposits (claystones, siltstones, and sandstones) from the Lower Carboniferous to Visean periods. The overlying strata include undeformed sedimentary rocks from the Cretaceous and Tertiary periods on the Kem Kem Plateau, capped by a continental Miocene complex and, further eastward, a Pliocene limestone cover on the Hamada du Guir (Benharref et al., 2014). The Quaternary epoch is marked by a diverse array of continental surface formations, including interlocked glacis-terrace systems, loamy, halomorphic, and sebkha soils, and a well-developed dune system. These formations, whether associated with elevated regions (glacis) or valleys (terraces, halomorphic soils, dunes), reflect the distinct climatic conditions characteristic of this sub-Saharan environment.

These varying surface roughness characteristics lead to distinct scattering mechanisms of synthetic aperture radar (SAR), enabling more precise delineation of geological units by incorporating lithological information obtained from multispectral sensors. Eight distinct class categories are clearly identified for the first time based on their polarization indices, Pauli decomposition, and polarization signatures:

Sand dunes. Aeolian sands correspond to mobile sandy accumulations and outcrop in the dunes of Erg Znaigui and Erg Chebi (**Fig. 11a**). The highest dunes attain an elevation of approximately 150 m above the surrounding plain. Locally, the dune crests exhibit random to volume diffusion, characterized by elevated HV values relative to other channels.

Clayey sandstone. They correspond in the field to the coarse-grained sandstones and conglomerates of the Upper Cretaceous period, the micaceous sandstones and pelites of the Upper Devonian period, and the sandstones and argillite-sandstones of the Tachilla formations, Bani Group, and upper Ktaoua formation of the Ordovician period (**Fig. 11b**). These deposits exhibit primarily dipolar diffusion at moderate entropy, characterized by a moderate correlation in the orientations of the scatterers. Additionally, the response shows a stronger maximum at VV polarization than at HH polarization, indicative of linear polarization.

Shale–sandstone. These formations, belonging to the Visean age, constitute the base of the Tafilalet plain. They comprise the Oued Znaïgui formation, characterized by 300-500 m of gray-green micaceous pelites and sandstones (**Fig. 11c**), the Mardani formation, consisting of 400-700 m of dark gray clayey shales intercalated with sandstone; and the Mougui-Ayoun formation, featuring sandstones intercalated with shales. The maximum response occurs at HH polarization, exceeding that at VV polarization. Notably, the maximum response shifts from the horizontal to vertical direction. Furthermore, the ellipticity angle of 0° signifies linear polarization.

Limestone and marl-limestone. They correspond to the limestone to marl-limestone sequence of the Upper Devonian of Tafilalet (Achguig Formation approximately 350 m thick in the reliefs west of Oued Ziz), the flint limestones, bedded limestones, and marls of the Upper Cretaceous of Kem Kem plateau (**Fig. 11b**), south of the study area, and the Pliocene limestone covering slab of the Hamada du Guir. The Pauli decomposition results reveal very strong multiple scattering and double rebound scattering, suggesting the presence of very rough and blocky surfaces.

Wind-blown Sand. These deposits are present in both the beds of wadis and secondary ravines, composed of pebbles and gravel with an unconsolidated silty-clay fraction to which a sandy fraction is added due to wind transport. This sandy contribution can evolve into small dunes depending on the strength of the wind and the presence of local obstacles (**Fig. 11d**). These deposits exhibit moderate entropy and a rougher surface consisting of more rugged and weathered rocks. In certain areas, these sands occupy relatively smooth open water surfaces, producing single-bounce scattering with more variation between all polarization responses.

Terrace sediments and salt crusts. These saline crusts, which are found in depressions filled by fine, highly saline sediments, are located within the Oued Ziz valley). Their accumulation is attributed to the combination of low precipitation and high evaporation rates. These facies exhibit low entropy and correspond to pure targets characterized by exposed soil and minimal surface roughness.

Water class. The water surfaces of the temporary lakes located west and north of Erg Chebbi display Bragg-type scattering, which indicates a Bragg scattering of signals.

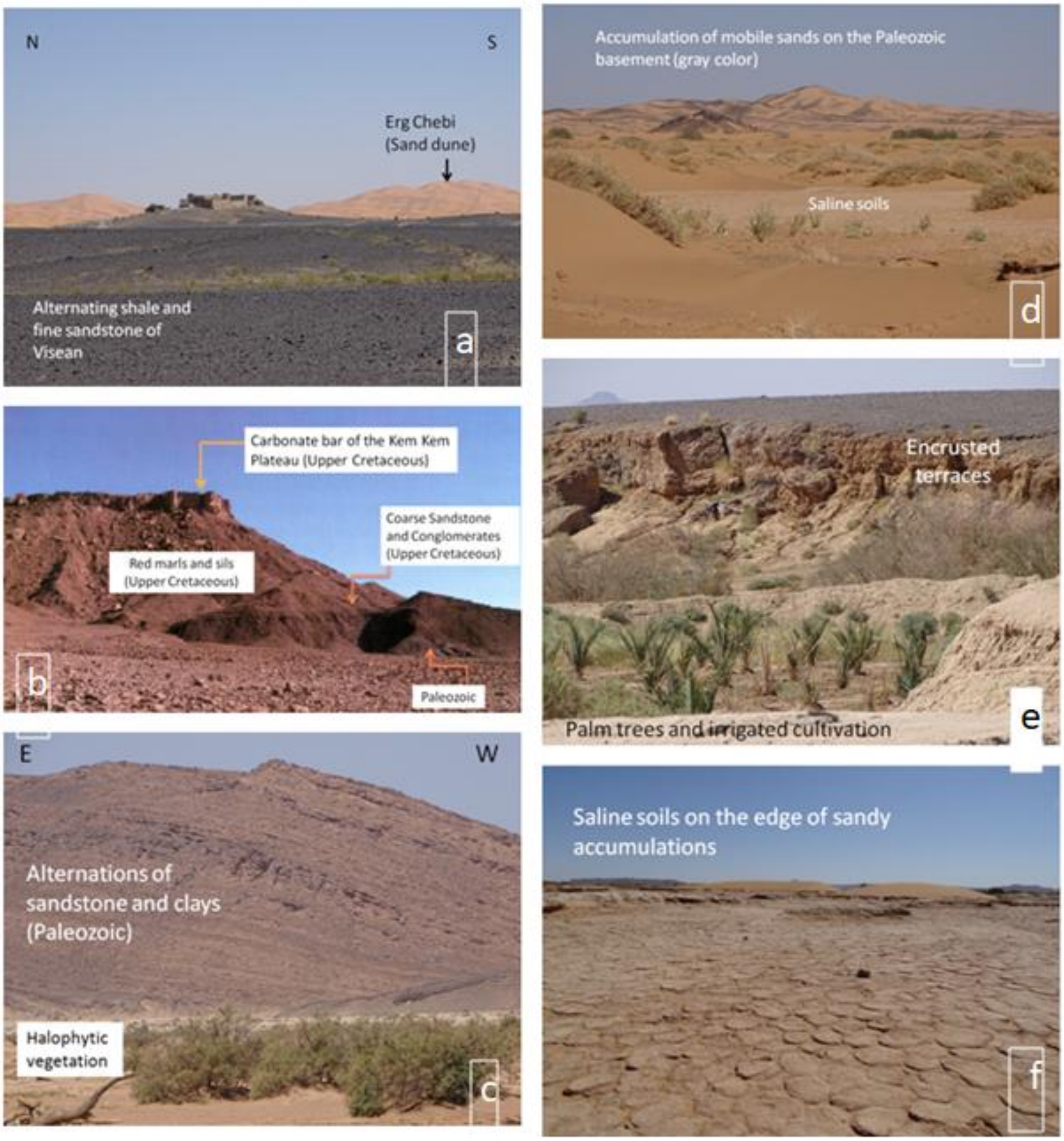

Fig. 11. Field photos of the different geological units along the study area.

Vegetation. This halophytic vegetation, encompassing samphire, tamarisk, palm trees, and irrigated cultivation, represents the natural flora that flourished in these narrow valleys. Essential to its development were the small water bodies and alluvial soil, which became enriched with organic matter over time.

It is noteworthy that the investigated terrains are situated within regions of moderate anisotropy (ranging from 0.32 to 0.36). Consequently, the surfaces under examination exhibit a propensity towards diffusion-dominated mechanisms, with an equivalent likelihood of manifestation on surfaces characterized by varying degrees of entropy.

6. CONCLUSION

In this study, surface land cover in the Tafilalet plain and surrounding areas was classified using ASTER and full-polarimetric SAR images. The integration of various polarimetric decomposition techniques significantly improved the classification results. Full-polarimetric data acquired by ALOS/PALSAR-2 demonstrated superior detection capabilities compared to optical imagery, providing clearer discrimination of lithological units, while ASTER images showed lower contrast and ambiguities due to spectral limitations and shadowing. Quantitative accuracy assessment was limited by the availability of ground-reference data.

The classification process employed L-band polarimetric signatures from ALOS/PALSAR-2, including decomposition into entropy, alpha, and anisotropy values, Alpha-Entropy analysis to identify dominant scattering mechanisms, Entropy-Anisotropy-Alpha color composites to examine the geometry of rock units, and Pauli decomposition to separate the three main scattering mechanisms. The supervised Wishart algorithm was applied as an object-based classifier.

For the first time in this arid desert region, polarimetric signatures were established for eight land cover classes, grouped into three roughness categories. Low-roughness surfaces include dry valleys and aeolian sand deposits, moderate-roughness surfaces correspond to sandstone–clay, shale, and limestone terrains, and very rough surfaces with multiple scattering are associated with sand dune ridges. These results highlight the strong potential of SAR polarization signatures for characterizing surface roughness and the morphological properties of geological units. The classification based on full-polarimetric SAR data showed a high consistency with official geological maps, demonstrating superior accuracy compared to optical image-based classification.

REFERENCES

Benharref, M., Alvaro, J.J., Hibt, M., Pouclet, A., El Hadi, H. & Boudad, L. (2014) Carte géologique du Maroc au 1/50 000, feuille Marzouga. *Notes et Mémoires du Service Géologique du Maroc*, No. 553, 119 p.

Boerner, W.M. (2004) Recent advances in radar polarimetry and polarimetric SAR interferometry. Paper presented at the *RTO SET Lecture Series on Radar Polarimetry and Interferometry*. http://dx.doi.org/10.1016/j.asr.2017.04.018

Boerner, W.M., Cloude, S.R., (2002) Radar polarimetry and interferometry: Past, present and future trends. *Proceedings of the XXVIIth General Assembly of the International Union of Radio Science (URSI)*, Maastricht Exhibition and Congress Centre, The Netherlands, 17–24 August 2002.

Boerner, W.M., et al. (1985) *Inverse Methods in Electromagnetic Imaging.* Proceedings of the NATO Advanced Research Workshop, Bad Windsheim, FR Germany, 18–24 September 1983, Parts 1 & 2, NATO-ASI C-143, D. Reidel Publishing Co. https://doi.org/10.1007/978-94-009-5271-3

Cloude, S.R. & Pottier, E. (1996) A review of target decomposition theorems in radar polarimetry. *IEEE Transactions on Geoscience and Remote Sensing*, 34(2), 498–518. https://doi.org/10.1109/36.485127

Cloude, S.R. & Pottier, E. (1997) An entropy-based classification scheme for land applications of polarimetric SAR. *IEEE Transactions on Geoscience and Remote Sensing*, 35, 68–78. https://doi.org/10.1109/36.551935

Cloude, S.R. (1999) Eigenvalue parameters for surface roughness studies. *Proceedings of SPIE – International Society for Optics and Photonics*, 3754, 2–13.

Cooley, T., Anderson, G.P., Felde, G.W., Hoke, M.L., Ratkowski, A.J., Chetwynd, J.H., Gardner, J.A., Adler-Golden, S.M., Matthew, M.W., Berk, A., Bernstein, L.S., Acharya, P.K., Miller, D. & Lewis, P. (2002) FLAASH, a MODTRAN4-based atmospheric correction algorithm, its application and validation. *Proceedings of the IEEE International Geoscience and Remote Sensing Symposium (IGARSS '02)*, 1413–1418. https://doi.org/10.1109/IGARSS.2002.1026134

Deschamps, G.A. (1951) Geometrical representation of the polarization of a plane electromagnetic wave. *Proceedings of the IRE*, 39, 540–544.

Destombes, J. & Hollard, H.C. (1975) Carte géologique du Maroc, Tafilalt–Taouz au 1/200 000. *Notes et Mémoires du Service Géologique du Maroc*, No. 244.

Joly, F. (1962) *Étude sur le relief du Sud-Est marocain.* Travaux de l'Institut Scientifique Chérifien, Série Géographie Physique, 10, Rabat, 578 p.

Lee, J.S. & Pottier, E. (2009) *Polarimetric radar imaging: From basics to applications.* CRC Press, New York. https://doi.org/10.1201/9781420054989

Lee, J.S., Grunes, M.R., Pottier, E. & Ferro-Famil, L. (2004) Unsupervised terrain classification preserving polarimetric scattering characteristics. *IEEE Transactions on Geoscience and Remote Sensing*, 42, 722–731. https://doi.org/10.1109/TGRS.2004.836769

Lee, J.S., Grunes, M.R. & Kwok, R. (1994) Classification of multi-look polarimetric SAR imagery based on complex Wishart distribution. *International Journal of Remote Sensing*, 15(1), 2299–2311. https://doi.org/10.1080/01431169408954244

Lee, J.S., Grunes, M.R., Ainsworth, T.L., Du, L.J., Schuler, D.L. & Cloude, S.R. (1999) Unsupervised classification using polarimetric decomposition and the complex Wishart classifier. *IEEE Transactions on Geoscience and Remote Sensing*, 37(5), 2249–2258. https://doi.org/10.1109/36.789621

Lee, J.S., Wen, J.H., Ainsworth, T., Chen, K.S. & Chen, A.J. (2008) Improved sigma filter for speckle filtering of SAR imagery. *IEEE Transactions on Geoscience and Remote Sensing*, 47, 202–213. https://doi.org/10.1109/TGRS.2008.2002881

López-Martínez, C. & Pottier, E. (2021) Basic principles of SAR polarimetry. In: Hajnsek, I. & Desnos, Y.-L. (eds.) *Remote Sensing and Digital Image Processing*, Vol. 25, 1–58. Springer, Cham. https://doi.org/10.1007/978-3-030-56504-6

Lu, D. & Weng, Q. (2007) A survey of image classification methods and techniques for improving classification performance. *International Journal of Remote Sensing*, 28, 823–870. https://doi.org/10.1080/01431160600746456

Mattia, F. & Le Toan, T. (1999) Backscattering properties of multi-scale roughness surfaces. *Journal of Electromagnetic Waves and Applications*, 13, 491–526. https://doi.org/10.1163/156939399X00240

Michard, A., Frizon de Lamotte, D., Liégeois, J.P., Saddiqi, O. & Chalouan, A. (2008) Conclusion: Continental evolution in western Maghreb. In: Michard, A., Saddiqi, O., Chalouan, A. & Frizon de Lamotte, D. (eds.) *Continental Evolution: The Geology of Morocco. Lecture Notes in Earth Sciences*, 119, 395–404. Springer, Berlin.

Oliver, C. & Quegan, S. (2004) *Understanding synthetic aperture radar images.* SciTech Publishing, Raleigh.

Qi, Z., Yeh, A.G.O., Li, X. & Lin, Z. (2012) A novel algorithm for land use and land cover classification using RADARSAT-2 polarimetric SAR data. *Remote Sensing of Environment*, 118, 21–39. https://doi.org/10.1016/j.rse.2011.11.001

Vanzyl, J.J., Zebker, H.A. & Elachi, C. (1987) Imaging radar polarization signatures: theory and observation. *Radio Science*, 22(4), 529–543. https://doi.org/10.1029/RS022i004p00529

Varghese, A.O. & Joshi, A.K. (2014) Polarimetric classification of C-band SAR data for forest density characterization. *Current Science*, 108(1), 100–106.

Woodhouse, I.H. (2006) *Introduction to microwave remote sensing.* Taylor & Francis, Boca Raton. https://doi.org/10.1201/9781315272573